Scale-dependent tipping points of bacterial colonization resistance

Yuya Karita[a,b], David T. Limmer[c,d,e], and Oskar Hallatschek[a,b,1]

[a]Department of Physics, University of California, Berkeley, CA 94720; [b]Department of Integrative Biology, University of California, Berkeley, CA 94720; [c]Department of Chemistry, University of California, Berkeley, CA 94720; [d]Kavli Energy NanoScience Institute, Berkeley, CA 94720; and [e]Chemical and Materials Science Divisions, Lawrence Berkeley National Laboratory, Berkeley, CA 94720

Edited by David Weitz, Department of Physics, Division of Engineering and Applied Science, Harvard University, Cambridge, MA; received August 23, 2021; accepted January 5, 2022

Bacteria are efficient colonizers of a wide range of secluded microhabitats, such as soil pores, skin follicles, or intestinal crypts. How the structural diversity of these habitats modulates microbial self-organization remains poorly understood, in part because of the difficulty to precisely manipulate the physical structure of microbial environments. Using a microfluidic device to grow bacteria in crypt-like incubation chambers of systematically varied lengths, we show that small variations in the physical structure of the microhabitat can drastically alter bacterial colonization success and resistance against invaders. Small crypts are uncolonizable; intermediately sized crypts can stably support dilute populations, while beyond a second critical length scale, populations phase separate into a dilute region and a jammed region. The jammed state is characterized by extreme colonization resistance, even if the resident strain is suppressed by an antibiotic. Combined with a flexible biophysical model, we demonstrate that colonization resistance and associated priority effects can be explained by a crowding-induced phase transition, which results from a competition between proliferation and density-dependent cell leakage. The emerging sensitivity to scale underscores the need to control for scale in microbial ecology experiments. Systematic flow-adjustable length-scale variations may serve as a promising strategy to elucidate further scale-sensitive tipping points and to rationally modulate the stability and resilience of microbial colonizers.

colonization resistance | microbiome stability | phase separation | active matter | microfluidics

Natural microbial communities are often found to be remarkably stable, capable of either quickly recovering from disturbances or remaining essentially unaffected by them (1–4). Stability is particularly puzzling in small populations, which are prone to number fluctuations and lack the size and extent to buffer against local environmental changes. Nevertheless, small but stable populations have been found in association with spatially defined microhabitats (4–10).

Strains that colonize cavities are sometimes found to be so stable that they hold their ground against even much fitter invaders (11). For example, *Bacteroides fragilis* is a particularly resilient colonizer of crypts in mouse guts (7). Conspecifics are unable to invade, unless the resident strain is strongly suppressed by an antibiotic. A similar colonization resistance has been demonstrated for groups of ceca microbiota in mice guts (9) and for *Lactobacillus plantarum* in fly guts (10, 12).

The ubiquity of microhabitat-associated stability and colonization resistance raises the question of whether these features generically emerge in confined spaces, for example, soil pores (13–15), skin follicles (4, 16), or crypts and folds in gut-like environments (5, 17, 18). Previous studies have identified biological features, such as suppressed biofilm growth or the expression of specific adhesion molecules, that promote stability in specific systems (1, 7, 19–21). However, we currently lack systematic scale-dependent measurements to identify a generic mechanism of stability and resilience in microhabitats, as well as a theory that could predict colonization success and tipping points. To fill this gap, we developed an approach to measure the scale dependence of microbial colonization patterns combined with a predictive theory of how microbes invade, occupy, and protect confined microhabitats.

Experimental Setup

Our experiments employ a microfluidic incubation device that allows us to continuously monitor bacterial population dynamics in crypt-shaped chambers across many length scales (Fig. 1*A*). A supply channel is used to continuously perfuse the device with media, enabling the experiments to run under constant conditions for several days. As bacteria are inoculated and pass through the supply channel, they get exposed to rectangular cavities of systematically varied depths (10 to 350 μm). Even though the fluid inside these cavities is largely stagnant, it is nutrient rich and hence, supports growth due to the rapid diffusion of small nutrient molecules from the supply channel (22, 23).

In this device, length scale–dependent ecological processes can be identified by comparing the colonization dynamics across the sequence of chambers. To capture the differential population dynamics in single microscopy frames, we ordered the cavities according to size (*SI Appendix*, Fig. S1 shows a randomized control). The device thus resembles a pan flute in appearance, so we refer to our device as a "microfluidic pan flute." We employed it

Significance

The commonly observed stability of natural microbiomes is important for their function, yet the ubiquity of microbiome stability remains enigmatic. The strongest form of stability, colonization resistance, protects residents against invaders and is often associated with specific porous structures, such as skin follicles or intestinal crypts. By systematically probing the colonization of fly gut–derived bacteria in microfluidic pores of varying sizes, we revealed that colonization patterns and invasion rates strongly depend on the pore size. Mathematical modeling shows that bacteria spontaneously tend to organize into a dense colonization-resistant state in pores exceeding a critical size. The scale dependence of stability and resilience could bias ecological filtering in microbiomes and should be considered in the design of microbial ecology experiments.

Author contributions: Y.K. and O.H. designed research; Y.K., D.T.L., and O.H. performed research; Y.K., D.T.L., and O.H. contributed new reagents/analytic tools; Y.K., D.T.L., and O.H. analyzed data; and Y.K., D.T.L., and O.H. wrote the paper.

The authors declare no competing interest.

This article is a PNAS Direct Submission.

[1]To whom correspondence may be addressed. Email: ohallats@berkeley.edu.

This article contains supporting information online at https://www.pnas.org/lookup/suppl/doi:10.1073/pnas.2115496119/-/DCSupplemental.

Published February 10, 2022.

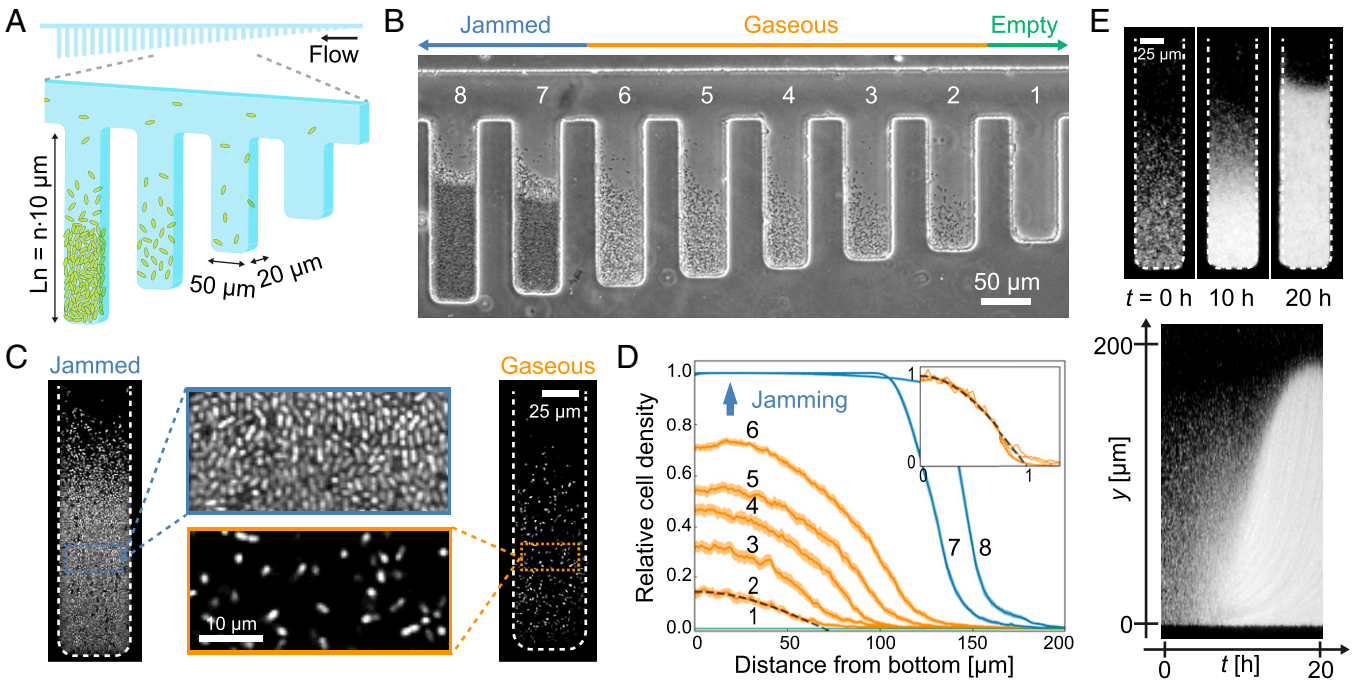

Fig. 1. Microfluidic experiments reveal length scale–dependent colonization patterns. (*A*) A scheme of our microfluidic pan flute incubation device. Rectangular cavities of systematically varied depths ($n = 1, 2, \ldots, 35$) are connected to a common supply channel through which media and bacteria flow. (*B*) The steady state after 5 d of incubation of a fly gut bacterium (*A. indonesiensis*). Depending on their length, cavities could not be invaded (1), hosted a gaseous population (2 to 6), or hosted a phase-separated population with a jammed and gaseous state (7 and 8). (*C*) Confocal images of a partially jammed and gaseous population. The zoomed-in images are magnifications of the zoomed-out snapshots. (*D*) Steady-state cell density profiles obtained from time-lapse movies. The shaded regions show the SEMs. The profiles of gaseous phases (orange) collapsed to our linearized establishment model (black) upon rescaling both axes (*Inset*). (*E*) A kymograph of the jamming front movement.

to explore the colonization dynamics of several bacterial genera, focusing mainly on *Acetobacter*, which is prevalent in the fly gut (10, 24) and grows aerobically.

Results

We found that the emerging population dynamics sensitively depend on the length of the incubation chamber (Fig. 1*B* and Movie S1). The scale sensitivity is particularly strong near two recognizable phase transitions:

Establishment Transition. While all cavities are sporadically visited by cells, colonization attempts remain unsuccessful in small chambers. In chambers exceeding a certain threshold length (170 µm in Fig. 1*B*), cell densities stabilize after 2 to 3 d of incubation and are maintained for at least 5 d. Cell densities, as measured from the time-averaged signal intensity, increase with chamber length, are highest at the floor of the cavities, and gradually decay toward a line of zero density (Fig. 1*D*). We call this regime "gaseous" because the cell packing fraction is small and cells diffuse almost freely (*SI Appendix*, Fig. S2).

Jamming Transition. When the chamber length exceeds a second threshold (220 µm in Fig. 1*B*), a densely populated region appears at the bottom of the cavities that is sharply separated from a gaseous region toward the opening of the cavities (chambers 6 and 7 in Fig. 1*B*). Confocal imaging shows that neighboring cells are in direct contact in the dense phase, which is why we call the condensed phase "jammed" (Fig. 1*C*). Dynamically, the jammed phase grows like a wave from the floor toward the open boundary of a chamber, as can be seen in the kymograph in Fig. 1*E*. The growth of this wave slows down near the jamming transition (Movie S1). Interestingly, the transition from gaseous to jammed is abrupt in the size of the chambers. Between two neighboring cavities, differing by just 5% in length, the colonization state transitions from gaseous to nearly 75% jammed (quantified in Fig. 1*D*).

We observed qualitatively similar colonization patterns for species of other genera, including *Vibrio cholerae* and *Lactococcus lactis* (*SI Appendix*, Fig. S3). We, therefore, sought to explain the pronounced length-scale sensitivity by a general species-independent mechanism.

Linear Establishment Model. The colonization of a cavity can be viewed as a tug-of-war between cell proliferation and cell removal by outflow or death.* This competition can be considered in the absence of regulation or specific cell–cell interactions in order to discern whether the rich scale-dependent phase behavior seen in our experiments is a consequence of general biophysical processes. To describe how the cell density $c(y,t)$ at a vertical position y and time t changes over time, we use the linear reaction–diffusion equation $\partial_t c(y,t) = D_0 \partial_y^2 c(y,t) + r\, c(y,t)$, where the first term represents cell diffusion with diffusivity D_0 and the second term represents cell proliferation with growth rate r. Since cells cannot penetrate the floor of the chamber, we use a reflecting boundary condition at $y = 0$, $\partial_y c(0,t) = 0$. We also introduce an absorbing boundary at $y = L$, where the cells are swept away by the media flow, $c(L,t) = 0$.

Our mathematical analysis (*SI Appendix*, section A.3) shows that the dynamics of the density profile can be decomposed into a sum of independently evolving normal modes. The empty state is stable if the amplitude of all normal modes shrinks, which requires that the scale L of the population does not exceed the critical scale $L_{\text{est}} = \pi\sqrt{D_0/r}/2$. In turn, this implies that bacteria can establish in a chamber only if

*In our experiments, removal is dominated by outflow. Cell death can also be included through an effective growth rate, representing the difference between growth and death rate.

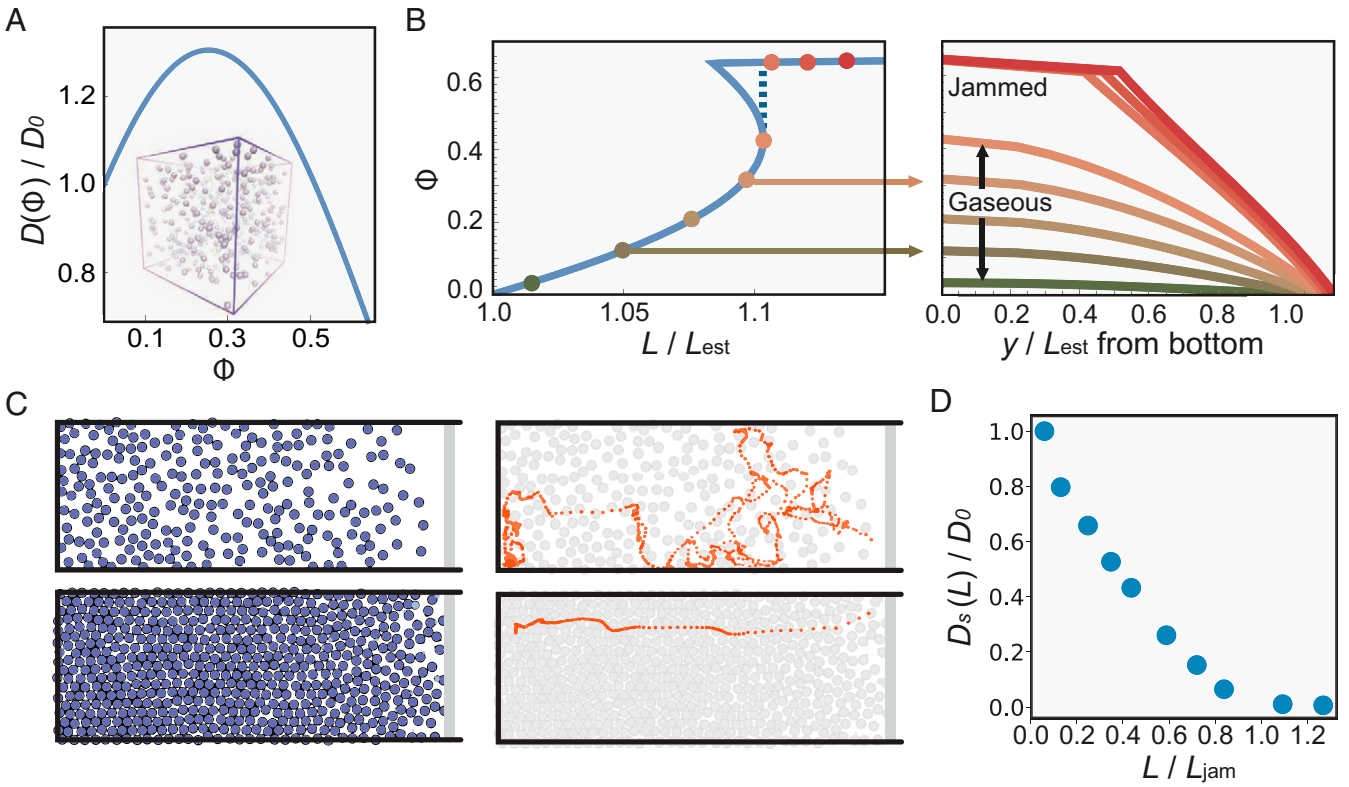

Fig. 2. A model of proliferating active matter shows that collective motion can stabilize a growing population and drive phase separation. (*A*) Simulations reveal that the collective diffusivity of an idealized model of proliferating hard spheres in suspension, as illustrated in the *Inset*, is nonmonotonic as a function of the packing fraction $\Phi = c\pi\sigma^3/6$, with σ the diameter of the particle. The negative gradients at high densities can drive a discontinuous transition toward jamming. (*B*) The packing fraction profile (*Right*) was computed from the density-dependent diffusivity in *A* (*SI Appendix*, section A.5). The maximum packing fraction (*Left*) shows a fold bifurcation as a function of L/L_{est}, resulting in a sudden transition to a (partially) jammed state. (*C*) Minimal simulations of proliferating soft disks and example tagged particle trajectories for gaseous $L < L_{\text{jam}}$ (*Upper*) vs. jammed states $L > L_{\text{jam}}$ (*Lower*) pores. (*D*) Self-diffusion, D_s, in the gaseous state is larger by orders of magnitude than in the jammed state, suggesting a mechanism for an invasion barrier.

$L > L_{\text{est}}$. Thus, establishment is promoted by increasing the growth rate or decreasing the diffusivity, which drives the cell leakage. Using the measured growth rate, $r \approx 0.33 \pm 0.01$ h^{-1} (*SI Appendix*, Fig. S4 *A* and *D*), and diffusivity, $D_0 \approx (0.37 \pm 0.01) \times 10^3$ μm^2/h (*SI Appendix*, Fig. S2), we estimate establishment in our experiments to occur at the scale $L_{\text{est}} \approx 53 \pm 1$ μm. This is consistent with the empirical value 53 ± 7 μm that we extrapolate from our measurements (*SI Appendix*, Fig. S5*B*). We also confirmed that the establishment length changes predictably with variations in growth rate (*SI Appendix*, Fig. S6). More importantly, the measured density profiles agree well with the cosine shape of the first normal mode, as observed in Fig. 1*D*, which is expected to dominate close to the onset of colonization (*SI Appendix*, section A.4). Our analysis is best suited to describe the bulk of the population where cell motion is dominated by diffusion. Deviations are expected and indeed, visible around the opening of cavities (near vanishing cell density) where the flow of the media is not negligible.

Nonlinear Population Control. Our linear model can tell us whether bacteria grow in empty chambers, but it remains blind to how a population of successful colonizers reaches a steady state with a finite population size and how stable this state is. To predict the long-term dynamics, we needed to include a (nonlinear) population control term that modulates the competition between cell proliferation and removal. For example, bacterial batch cultures are often limited by nutrient deprivation or waste product accumulation, implying that the growth rate is not constant but decays with density (logistic population control). However, growth rates in the jammed and dilute phases were statistically indistinguishable (*SI Appendix*, Fig. S4), suggesting that nutrient deprivation did not limit population growth. Therefore, we hypothesized that, while the growth rate remains approximately constant, the population outflow adjusts itself via a density-dependent diffusivity $D(c)$. Steady state is reached when the cell leakage matches the influx of newborn cells in the bulk of the chamber.

Crowding-Induced Phase Transition. Our mathematical analysis shows that a monotonically increasing $D(c)$ (more cells $\rightarrow$ more outflow) is capable of stabilizing a gaseous state inside the chambers (*SI Appendix*, section A.4). However, to reproduce a sudden jamming transition, $D(c)$ has to have an extended region of sufficiently negative slope at high densities (more cells $\rightarrow$ less outflow). Intuitively, this generates a positive feedback cycle. As the density fluctuates up, diffusion-induced outflow goes down, which leads to even higher cell densities, suppressing outflow even more and so on. The cycle only breaks when the bacteria jam and come into contact, upon which the bulk modulus and hence, $D(c)$ shoot up by several orders of magnitude (25).

The required negative slope of $D(c)$ could be induced at high density by constitutive or crowding-induced stickiness between cells or active motility, which has been shown to drive phase separation (26). Our simulations (Fig. 2) and analytical arguments (*SI Appendix*, section A.7) show that even purely repulsive nonmotile spheres exhibit a qualitatively similar phase behavior as seen in our experiments. Thus, a transition between gaseous and partially jammed states emerges without any special biotic factors other than proliferation.

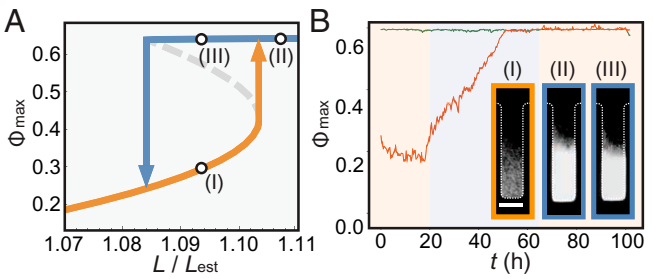

Fig. 3. Bistability near the tipping point. (*A*) Phase diagram. The maximal packing fraction at steady state, Φ_{max}, as predicted from the density-dependent diffusivity in Fig. 2*A*. When the control parameter L/L_{est} is gradually increased, the state of the system suddenly jumps from a gaseous (I) to a partially jammed state (II; arrow pointing up). If one decreases the control parameter again, the system jumps back to a gaseous state (arrow pointing down) but at a different value of the control parameter, implying a hysteresis and a region of bistability. (*B*) Experiments to test bistability. A flow decrease triggered in the depicted chamber the transition from gaseous (I) to jammed (II) via an effective increase of the habitat size *L*. The orange curve depicts the density increase over time. After saturation, we increased the flow again, but the chamber remained in the jammed state (III) at high density. On the other hand, no bistability was observed in a deeper chamber (green curve). To define the packing fraction on the *y* axis, the relative cell density (shown in *SI Appendix*, Fig. S7) was normalized by the random close packing of monodisperse spheres, $\Phi_{rcp} \sim 0.64$. (Scale bar: 50 μm.)

In *SI Appendix*, we show that, by exploiting a mathematical analogy to a solvable Newtonian problem, the phase diagram and the density profiles (c.f. Fig. 2*B* for hard spheres) can be obtained exactly by numerical integration (via *SI Appendix*, Eqs. **34** and **35**) from the underlying growth and dispersal parameters. This analysis shows that the position of the tipping points depends on the entire functions $D(c)$ and $r(c)$ up until the tipping point and thus, can be modulated by any means that change these functions, such as attractive interactions or quorum sensing.

Our theory also predicts that the jamming transition arises through a fold bifurcation and therefore, should have the characteristics of a tipping point (27–29). In particular, after a chamber becomes jammed, it is not easily unjammed and requires a substantial perturbation of the control parameters (growth rate or diffusivity). This also implies that there must be a region of bistability, where in the same chamber, two states are stable—one gaseous state and one phase-separated state (Fig. 3*A*). We confirmed that, in our experiments, chambers near the jamming transition indeed show bistability (Fig. 3*B* and *SI Appendix*, Fig. S7) by flipping from one state to another using flow modulation (*SI Appendix*, Fig. S8).

Tipping points also reveal themselves dynamically through a dramatic slowing down near the transition point—a phenomenon called critical slowing down (27). Indeed, time-lapse Movie S1 shows that the relaxation dynamics near the transition point becomes very slow. The smallest jammed chamber takes about 30 h or 14 doubling times to reach steady state, compared with 6 h or less in the largest chambers.

Crowding-Induced Drop in Diffusion. Simulations of a proliferating soft sphere model (*SI Appendix* has details) further show that the cellular self-diffusion is dramatically reduced upon jamming, consistent with an onset of rigidity, except for movement of order one-cell diameter per doubling induced by the division process (Fig. 2*C*). While in our experiments, we could not track single cells in the jammed phase, we could track lineages using fluorescent tracers (*SI Appendix*, Fig. S9), which also suggests that self-diffusion drops by two orders of magnitude from the gaseous to the jammed state.

A drop in self-diffusion has important consequences for species invasions. It lowers the chance for outside cells to diffusively penetrate the jammed fraction against the proliferation current coming from the floor of the chamber. Accounting for this crowding-induced diffusion barrier in a theory of strain invasion (*SI Appendix*, section C.1), we predict that the rate at which an external strain invades a jammed resident population is exponentially small in the ratio of the thickness of the jammed phase and the cell diameter. Thus, invasion of jammed populations should be an extremely rare event.

Colonization Resistance. To test this prediction, we performed specific invasion experiments. We inoculated our device with the wild-type strain of *Acetobacter indonesiensis* and waited until a steady state was reached. We then flowed in a sister strain of the same species, which was fluorescently labeled green and resistant to the drug tetracycline. Titration of tetracycline then allowed us to tune the growth rate advantage of the invading strain.

In the absence of antibiotics, we did not observe any successful invasion over the experimental timescale of 5 d. When we added 10 μg/mL of the antibiotic (60% of MIC), scale-dependent invasion dynamics ensued. In the initial 24 h, the drug-sensitive populations decreased the population density (Movie S3), thus shifting the phase boundary between gaseous and jammed to larger cavities. Over the next 48 h, drug-resistant cells entered and seized a substantial number of the gaseous chambers (Fig. 4*C* and Movie S4). Upon successful invasion, the population density generally increased again. Importantly, while most of the gaseous chambers were ultimately invaded, none of the jammed chambers were (of seven colonized pan flutes monitored over 2 to 5 d in three independent experiments). The primary effect of the antibiotic is to push the state of some of the chambers from jammed to gaseous, upon which invasion becomes possible (Fig. 4*A*). Thus, while crowding strongly protects jammed populations from invasion, residents can be dislodged nevertheless if they are driven past a tipping point into a more fragile (gaseous) ecological state.

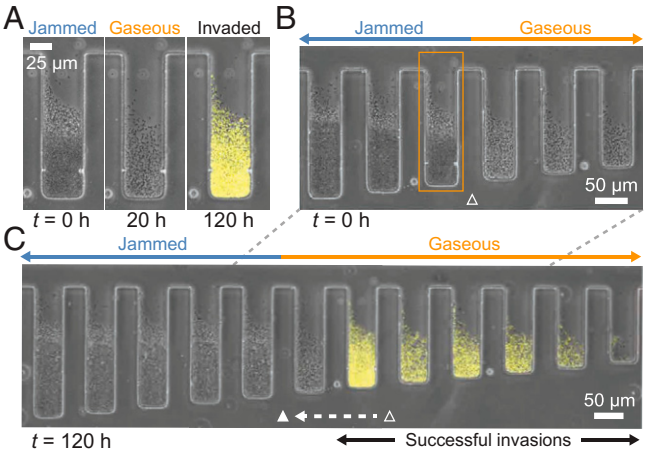

Fig. 4. Crowding-induced colonization resistance. (*A*) After the chambers were precolonized by the wild-type strain (dark), we introduced a fluorescently labeled "invader" strain (yellow). To make invasions more likely, we also increased the fitness of the invader by the simultaneous injection of an antibiotic (tetracycline) to which the invader was made resistant. (*B*) A steady state of sensitive populations before the invaders were inoculated. The unfilled triangle shows the transition point between jammed and gaseous phases in the experiment. The transition was manually defined based on the bright-field darkness of the populations. *C* shows 120 h after tetracycline was added to the culture medium. Drug-sensitive populations (dark) that remained jammed were not invaded. The unfilled and filled triangles show the transition points between jammed and gaseous phases at $t = 0$ h and $t = 120$ h, respectively. The injection of the growth inhibitor (tetracycline) shifted the transition point.

Discussion

We have shown that microbial colonization patterns can vary dramatically with the physical structure of their microenvironment. In particular, a crowded state with pronounced colonization resistance can arise spontaneously when the incubation scale exceeds a certain tipping point. Once pushed beyond the tipping point, it requires a substantial perturbation to break the ensuing colonization resistance, for instance, by using antibiotics to trigger the reverse transition toward a gaseous phase with increased mixing (Fig. 4*A*).

The physical structure of the microenvironment thus acts as an ecological filter, permitting stable and resilient colonization by species with matching traits. By modulating the physical characteristics of this filter, hosts can actively or passively shape the pool of potential bacterial residents. Modulating endogenous microstructures or introducing rationally designed structures may also be considered as a strategy for precision microbiome therapies to modulate microbial diversity.

The structure-induced stability supports the view that community assembly from potential colonizers is shaped by priority effects; whoever invades first enjoys colonization resistance against late invaders. The randomness induced by the order of strain arrival might contribute to the substantial host-to-host variability seen in some host-associated microbial communities (9, 16).

Colonization patterns, tipping points, and colonization resistance could be captured by a minimal model of proliferating active matter, which accounts for growth, diffusion, and leakage. This model revealed a generic fold bifurcation generating a discontinuous transition between a gaseous phase, in which cells diffuse freely, and a glassy, jammed phase. This transition differs from what is known as motility-induced phase separation (MIPS) (26) in the field of active matter (30, 31). MIPS is associated with a spinodal instability that arises when an effective diffusivity becomes negative—an unintuitive consequence of the nonequilibrium nature of active motility (32). In our case, the transition is triggered by the weaker condition of a (sufficiently) negative density-dependent diffusivity, which generically arises even for passively diffusing particles (33), for example, hard spheres. It would be interesting to extend our model of proliferating active matter by active motility to see how bacteria that grow and swim self-organize in confined spaces.

While the tipping points in our experiments could be explained by our minimal model, we expect that, in general, additional biotic and abiotic factors influence colonization patterns quantitatively. For example, crowding will be promoted if cells stick to one another directly or indirectly through biofilm formation or if nutrients are supplied from the floor of the chamber. On the other hand, both establishment and jamming tend to be hindered by strong nutrient limitations or bacterial motility. While further research is needed to explore the relative importance of these factors, their impact may be anticipated theoretically using a reaction–diffusion model, which entails a flexible approach to analyze steady states (*SI Appendix*, section A.5).

More broadly, our results underscore that the length scale of experimentation can have a strong influence on microecological processes, which could confound experiments that do not control for scale variation (34)—a well-appreciated problem in the macroecological context (35–37). Flow-tunable scale variations as implemented in our microfluidic pan flute offer a systematic experimental approach to detect or exclude scale sensitivity in culturable microbial communities. Since the timescales of microbial evolution and ecology are intertwined, we expect such scale-sensitive experiments to be an exciting avenue for future ecoevolutionary research (38).

Materials and Methods

Bacterial Strains and Culture Condition. The *A. indonesiensis* strains were derived from the strain named SB003 (gift from William Ludington, Carnegie Institution for Science), which was originally isolated from laboratory flies (*Drosophila melanogaster*) (10, 24). SB003 was transformed with a modified green fluorescent protein (mGFP5) via the backbone plasmid pCM62 (39) by Benjamin Obadia (12). For culturing, all strains were grown in de Man, Rogosa, and Sharpe (MRS) medium (BD) at 30 °C. Strains are selected with 15 μg/mL tetracycline (Corning Cellgro) if needed.

Microfluidics Fabrication. The microfluidic devices were fabricated by soft lithography (40). In order to make a master mold, a 20-μm-thick layer of negative photoresist (SU8-2010; MicroChem) was spin coated on a silicon wafer (WaferNet) and patterned by photolithography with a mask aligner (Hybralign 200; OAI) through a photomask (CAD/Art Services). On the master mold, polydimethylsiloxane (PDMS; Sylgard 184; Dow Corning) was poured with cross-linker at a 10:1 ratio and cured at 60 °C in an oven overnight. The patterned PDMS was punched to make holes for inlets and outlets. The PDMS was bonded to a glass coverslip with O_2 plasma treatment by a reactive ion etcher (Plasma Equipment Technical Services).

Microfluidic Cell Culture. Prior to microfluidic culture, cells were streaked on a plate from frozen stock and grown in a test tube with 3 mL MRS for 1 to 2 d. The suspension of cells was injected into a microfluidic device and cultured for 3 to 5 d with a continuous supply of the fresh medium until the system reached a steady state. The temperature was regulated at 30 °C by a microscope incubator (H201-T and UNO; Okolab), and the flow rate of the culture medium was controlled at 0.3 μL/h by syringe pumps (neMESYS; CETONI). Images were taken by inverted microscopes (IX81; Olympus [also, Eclipse Ti; Nikon was occasionally used for *SI Appendix*, Figs. S6*B* and S7*B*]) and a confocal microscope (LSM 700; ZEISS).

Density Profile Measurement. To quantitatively measure the density profile of cellular populations in microfluidic crypts, GFP-tagged cells were cultured in a microfluidic pan flute for about 3 d. After the system reached a steady state, fluorescent intensities were measured every 20 min for 14 to 48 h. The intensities were first averaged over the horizontal direction and then averaged over the time points at each y position. They were scaled by the intensity of jammed populations to get relative cell densities. An SEM was calculated by dividing the SD across time points by the square root of the approximate number of uncorrelated time points. The latter was estimated by dividing the total duration of the time-lapse movie by the typical relaxation time (6 h) of the density profile measured in the gaseous phase (*SI Appendix*, Fig. S7*D*).

Neutral Competition and Invasion with Fitness Effect. To observe competitions of two strains with and without fitness effects, wild-type and GFP-tagged strains were cocultured. As the GFP-tagged strain was resistant to tetracycline, with 10 μg/mL of tetracycline, the GFP-tagged cells grew normally, while the wild-type strain grew slowly. We confirmed that there was no significant growth rate difference between the strains in the absence of antibiotics (*SI Appendix*, Fig. S4*B*).

For neutral competition experiments, a 50:50 mixture of dark and GFP-tagged cells was inoculated into a microfluidic pan flute device and cultured for 2 d. As each type of cell colonized chambers stochastically, we parallelized six rows of the pan flutes and selected chambers with a desired initial population ratio. The population dynamics were observed with a fluorescent microscope every 20 min for a day.

To test the colonization resistance of jammed populations, we first cultured wild-type cells in a microfluidic device. After the populations reached a steady state, the culture medium was changed from MRS to MRS + 10 μg/mL tetracycline, and GFP-tagged cells were continuously flowed into the device. The resulting population decay and invasion dynamics were observed with a microscope every 20 min for 2 d. In addition, the snapshots of the populations were taken every day for 5 d.

Flow and Temperature Change Experiments. To investigate the effect of the system's parameters on the population density in microfluidic crypts, we dynamically changed the flow rate to tune the effective chamber depth. We initially cultured cells at a 0.8-μL/h flow rate for 3 d until the system reached a steady state and then, changed the flow rate to 0.3 μL/h. The decrease of the flow rate affected how deep the streamlines invaded chambers and changed the effective chamber depth by 5 to 10 μm (*SI Appendix*, Fig. S8). After the system reached a second steady state, we recovered the flow rate to 0.8 μL/h to investigate hysteresis.

We also dynamically changed the temperature of the incubation chamber to control the growth rate of cells. We first cultured cells at 22 °C, where the growth rate is 0.28 h^{-1}, until a steady state and ramped up the temperature to 30 °C, where the growth rate is 0.33 h^{-1} (the growth rate measurement is shown in *SI Appendix*, Fig. S4*D*). Then, we decreased the temperature

back to 22 °C. The transition dynamics were recorded every 20 min with a microscope (*SI Appendix,* Fig. S6*B*). Similarly, the temperature control between 26 and 30 °C was investigated (*SI Appendix,* Fig. S6*A*).

Colonization Experiments with Other Species. Colonization dynamics in a microfluidic pan flute were tested with various microbial species (*Escherichia coli*, *Bacillus subtilis*, *V. cholerae*, *Acetobacter pasteurianus*, *Acetobacter tropicalis*, and *L. lactis*; *SI Appendix*, Table S1 shows the strain details and culture media). Cells were streaked on a plate from frozen stock, and a small number of cells from a single colony were grown in a test tube with 3 mL of a culture medium for 1 to 2 d at 37 °C for *E. coli* and 30 °C for the other species. The cell suspension was injected into a microfluidic pan flute and cultured for 5 to 6 d with a continuous supply of fresh media until the system reached a steady state. During the microfluidic culture, the temperature was regulated at 30 °C for all species.

Growth Rate Measurement. The growth rate of cells was measured in two ways: growth assay with a plate reader and particle image velocimetry (PIV) of a jammed population on microfluidics. Prior to the measurements, cells were cultured in test tubes from single colonies for 1 to 2 d in MRS at 30 °C up to saturation. For the plate reader experiments, cell suspensions were diluted to 0.02 optical density (OD), and 200 μL of the suspensions were transferred to transparent flat-bottom 96-well plates (Thermo Fisher Scientific). The plates were incubated in a plate reader (Spectramax) at 30 °C, and the OD was measured at the 600-nm wavelength every 5 min with 30-s mixing before each measurement. The maximum growth rate was calculated by fitting an exponential curve to the initial 2-h growth. The growth rate of *A. indonesiensis* was measured as $0.325 \pm .003\ \mathrm{h}^{-1}$ (*SI Appendix*, Fig. S4*A*).

For the PIV measurement on microfluidics, cells were injected into a microfluidic device and incubated in a tabletop incubator until cells colonized chambers and formed stable populations. Bright-field images were taken every 3 min for 3 h and analyzed with PIVlab in MATLAB (41). PIV calculated the displacements of cells per time frame. The displacement of a cell at position $y = y_0$ was caused by the growth of cells at $y \in [0, y_0]$, and therefore, the displacement at position $y = y_0$ could be formulated as $d(y_0) = y_0(e^{r\Delta t} - 1)$. Since our time frame ($\Delta t = 3$ min) was much smaller than the doubling time of the cell (2.1 h), it held that $d(y_0)/\Delta t \approx r y_0$. Thus, the slope of the velocity field in the y direction gave the growth rate. The growth rate of *A. indonesiensis* was measured as $0.332 \pm .007\ \mathrm{h}^{-1}$ (*SI Appendix*, Fig. S4*D*).

Diffusivity Measurements.

Self-diffusivity. To estimate the self-diffusivity of cells in gaseous and jammed phases, the displacement of cells was tracked over time, and the mean square displacements were calculated. A 50:50 mixture of dark and GFP-tagged cells was injected in a microfluidic pan flute and cultured until the system reached a steady state. The motions of GFP-tagged cells were recorded with a fluorescent microscope every 30 s for 10 min for gaseous phases and every 20 min for 20 h for jammed phases. The displacement of cells in gaseous phases was automatically tracked with TrackMate in Fiji (42), and that in jammed phases was manually tracked with the Manual Tracking plugin of ImageJ.

Collective diffusivity. To determine the collective diffusivity, we adapted the Boltzmann–Matano analysis (43) to the present case of a reaction–diffusion system. Under the assumption that our general reaction–diffusion model, $\partial_t c(y,t) = \partial_y[D(c(y,t))\partial_y c(y,t)] + rc(y,t)$, is valid, we can express the density-dependent diffusivity $D(c)$ in terms of the steady-state density profile as follows:

$$D(c(y)) = \frac{r\int_0^y c(y')dy'}{-\partial_y c(y)}. \quad [1]$$

This equation allows us to estimate $D(c)$ from the exponential growth rate and the steady-state density profiles. The steady-state density profiles were determined from the temporal average of the fluorescent intensity of time-lapse movies. For the data in *SI Appendix*, Fig. S2*C*, we averaged the density profile over 20 frames (7 h) and locally approximated it with a quadratic function by the Savitzky–Golay method (44) to extract $\partial_y c(y)$. We excluded the y region 20% from the opening where the flow impacted the tail of the density profile and excluded the y region 20% from the bottom where $(\partial_y c(y))^{-1}$ was diverging.

Fluid Dynamics Simulations. The fluid dynamics of the culture medium flow through the cavity structures of our microfluidic devices were simulated using COMSOL. As a simple geometry, we defined a 500 × 50 × 20-μm supply channel with a 50 × 150 × 20-μm cavity in the middle. The fluid dynamics was modeled as incompressible Stokes flow subject to no-slip boundary conditions at the walls and a constant flow rate. To see how the flow field depends on external control parameters, we varied the depth of the cavity (30 to 150 μm) and the flow rate (100- and 250-μm/s mean flow rate).

Data Availability. Data and codes are available in GitHub at https://github.com/Hallatscheklab/PanfluteTippingPoints.

ACKNOWLEDGMENTS. We thank all members of the laboratory of O.H. for helpful discussions, Carl F. Schreck for useful discussion about early-stage agent-based simulations, and Arolyn Conwill and Tami Lieberman for their insightful and helpful comments. The *Acetobacter* strains were gifts from William B. Ludington, whom we also thank for useful discussions at the outset of the project. Research reported in this publication was supported by National Institute of General Medical Sciences of NIH Award R01GM115851, NSF CAREER Award 1555330, and the Miller Institute for Basic Research in Science. The hydrodynamics simulations were done in the Molecular Graphics and Computation Facility, University of California, Berkeley (NIH Grant S10OD023532). D.T.L. was supported by NSF Grant CHE-195458.

1. B. S. Griffiths, L. Philippot, Insights into the resistance and resilience of the soil microbial community. *FEMS Microbiol. Rev.* **37**, 112–129 (2013).
2. C. A. Lozupone, J. I. Stombaugh, J. I. Gordon, J. K. Jansson, R. Knight, Diversity, stability and resilience of the human gut microbiota. *Nature* **489**, 220–230 (2012).
3. K. Z. Coyte, J. Schluter, K. R. Foster, The ecology of the microbiome: Networks, competition, and stability. *Science* **350**, 663–666 (2015).
4. J. Oh, A. L. Byrd, M. Park, H. H. Kong, J. A. Segre; NISC Comparative Sequencing Program, Temporal stability of the human skin microbiome. *Cell* **165**, 854–866 (2016).
5. G. P. Donaldson, S. M. Lee, S. K. Mazmanian, Gut biogeography of the bacterial microbiota. *Nat. Rev. Microbiol.* **14**, 20–32 (2016).
6. T. Pédron *et al.*, A crypt-specific core microbiota resides in the mouse colon. *MBio* **3**, e00116–e12 (2012).
7. S. M. Lee *et al.*, Bacterial colonization factors control specificity and stability of the gut microbiota. *Nature* **501**, 426–429 (2013).
8. A. Saffarian *et al.*, Crypt-and mucosa-associated core microbiotas in humans and their alteration in colon cancer patients. *MBio* **10**, e01315–e01319 (2019).
9. I. Martínez *et al.*, Experimental evaluation of the importance of colonization history in early-life gut microbiota assembly. *eLife* **7**, e36521 (2018).
10. B. Obadia *et al.*, Probabilistic invasion underlies natural gut microbiome stability. *Curr. Biol.* **27**, 1999–2006.e8 (2017).
11. T. D. Lawley, A. W. Walker, Intestinal colonization resistance. *Immunology* **138**, 1–11 (2013).
12. R. Dodge *et al.*, A gut commensal niche regulates stable association of a multispecies microbiota. bioRxiv [Preprint] (2021). https://doi.org/10.1101/2021.09.30.462663 (Accessed 23 January 2022).
13. L. Ranjard, A. Richaume, Quantitative and qualitative microscale distribution of bacteria in soil. *Res. Microbiol.* **152**, 707–716 (2001).
14. V. Torsvik, L. Øvreås, Microbial diversity and function in soil: From genes to ecosystems. *Curr. Opin. Microbiol.* **5**, 240–245 (2002).
15. G. L. Grundmann, Spatial scales of soil bacterial diversity—The size of a clone. *FEMS Microbiol. Ecol.* **48**, 119–127 (2004).
16. A. Conwill *et al.*, Anatomy promotes neutral coexistence of strains in the human skin microbiome. *Cell Host Microbe*, 10.1016/j.chom.2021.12.007 (2022).
17. C. Tropini, K. A. Earle, K. C. Huang, J. L. Sonnenburg, The gut microbiome: Connecting spatial organization to function. *Cell Host Microbe* **21**, 433–442 (2017).
18. A. M. Mowat, W. W. Agace, Regional specialization within the intestinal immune system. *Nat. Rev. Immunol.* **14**, 667–685 (2014).
19. D. Or, B. F. Smets, J. Wraith, A. Dechesne, S. Friedman, Physical constraints affecting bacterial habitats and activity in unsaturated porous media—a review. *Adv. Water Resour.* **30**, 1505–1527 (2007).
20. K. Z. Coyte, H. Tabuteau, E. A. Gaffney, K. R. Foster, W. M. Durham, Microbial competition in porous environments can select against rapid biofilm growth. *Proc. Natl. Acad. Sci. U.S.A.* **114**, E161–E170 (2017).
21. C. Yang, K. M. Ottemann, Control of bacterial colonization in the glands and crypts. *Curr. Opin. Microbiol.* **47**, 38–44 (2019).
22. P. Wang *et al.*, Robust growth of *Escherichia coli*. *Curr. Biol.* **20**, 1099–1103 (2010).
23. G. Lambert, E. Kussell, Memory and fitness optimization of bacteria under fluctuating environments. *PLoS Genet.* **10**, e1004556 (2014).
24. R. Yamada, S. A. Deshpande, K. D. Bruce, E. M. Mak, W. W. Ja, Microbes promote amino acid harvest to rescue undernutrition in *Drosophila*. *Cell Rep.* **10**, 865–872 (2015).
25. E. K. Chu, O. Kilic, H. Cho, A. Groisman, A. Levchenko, Self-induced mechanical stress can trigger biofilm formation in uropathogenic *Escherichia coli*. *Nat. Commun.* **9**, 4087 (2018).
26. M. E. Cates, J. Tailleur, Motility-induced phase separation. *Annu. Rev. Condens. Matter Phys.* **6**, 219–244 (2015).
27. C. Wissel, A universal law of the characteristic return time near thresholds. *Oecologia* **65**, 101–107 (1984).
28. E. H. van Nes, M. Scheffer, Slow recovery from perturbations as a generic indicator of a nearby catastrophic shift. *Am. Nat.* **169**, 738–747 (2007).
29. L. Dai, D. Vorselen, K. S. Korolev, J. Gore, Generic indicators for loss of resilience before a tipping point leading to population collapse. *Science* **336**, 1175–1177 (2012).

30. S. Ramaswamy, The mechanics and statistics of active matter. *Annu. Rev. Condens. Matter Phys.* **1**, 323–345 (2010).
31. M. C. Marchetti *et al.*, Hydrodynamics of soft active matter. *Rev. Mod. Phys.* **85**, 1143 (2013).
32. M. E. Cates, D. Marenduzzo, I. Pagonabarraga, J. Tailleur, Arrested phase separation in reproducing bacteria creates a generic route to pattern formation. *Proc. Natl. Acad. Sci. U.S.A.* **107**, 11715–11720 (2010).
33. W. B. Russel, W. Russel, D. A. Saville, W. R. Schowalter, *Colloidal Dispersions* (Cambridge University Press, 1991).
34. J. Ladau, E. A. Eloe-Fadrosh, Spatial, temporal, and phylogenetic scales of microbial ecology. *Trends Microbiol.* **27**, 662–669 (2019).
35. J. A. Wiens, Spatial scaling in ecology. *Funct. Ecol.* **3**, 385–397 (1989).
36. S. A. Levin, The problem of pattern and scale in ecology: The Robert H. Macarthur award lecture. *Ecology* **73**, 1943–1967 (1992).
37. S. R. J. Ross *et al.*, Illuminating the intrinsic and extrinsic drivers of ecological stability across scales. *Ecol. Res.* **36**, 364–378 (2021).
38. V. Dakos *et al.*, Ecosystem tipping points in an evolving world. *Nat. Ecol. Evol.* **3**, 355–362 (2019).
39. C. J. Marx, M. E. Lidstrom, Development of improved versatile broad-host-range vectors for use in methylotrophs and other Gram-negative bacteria. *Microbiology (Reading)* **147**, 2065–2075 (2001).
40. J. C. McDonald *et al.*, Fabrication of microfluidic systems in poly(dimethylsiloxane). *Electrophoresis* **21**, 27–40 (2000).
41. W. Thielicke, E. J. Stamhuis, PIVlab-time-resolved digital particle image velocimetry tool for MATLAB, Version 3. https://figshare.com/articles/code/PIVlab_version_1_35/1092508/3. Accessed 23 January 2022.
42. J. Y. Tinevez *et al.*, TrackMate: An open and extensible platform for single-particle tracking. *Methods* **115**, 80–90 (2017).
43. C. Matano, On the relation between the diffusion-coefficients and concentrations of solid metals. *Jpn. J. Physiol.* **8**, 109–113 (1933).
44. A. Savitzky, M. J. Golay, Smoothing and differentiation of data by simplified least squares procedures. *Anal. Chem.* **36**, 1627–1639 (1964).